THE JOURNAL OF PHYSICAL CHEMISTRY LETTERS
A JOURNAL OF THE AMERICAN CHEMICAL SOCIETY

pubs.acs.org/JPCL

Letter

Complex Resonant Scattering Behavior in the Surface Plasmon Resonance Imaging Microscopy of Single Gold Nanorods

Yunshan Fan, Yara Aceta, Esther Hessong, Athena Bengston, Laris A. Biageyian, Quan P. Huynh, and Robert M. Corn*

Cite This: *J. Phys. Chem. Lett.* 2021, 12, 2004–2010

Read Online

ACCESS | Metrics & More | Article Recommendations | Supporting Information

ABSTRACT: Diffraction patterns observed in surface plasmon resonance imaging (SPRI) microscopy measurements of single gold nanorods (AuNRs) exhibit a complex behavior at wavelengths near the longitudinal plasmonic resonance band. SPRI microscopy measurements at 814 nm from AuNRs in three samples with resonance extinction maxima at 670, 816, and 980 nm reveal a variety of diffraction patterns with central peaks that are either positive, negative, or biphasic. A unitless ratio parameter M_R $(-1 \leq M_R \leq 1)$ is created to describe the distribution of diffraction patterns. A purely negative $(M_R = -1)$ central peak is observed for 30%, 57%, and 98% of the diffraction patterns in the 670, 816, and 980 nm samples, respectively. These results along with a theoretical modeling of the diffraction patterns with an anisotropic complex scattering coefficient suggests that this behavior only occurs for AuNRs when the laser wavelength used in SPRI experiments is shorter than the AuNR plasmonic resonance maxima, that is, in the anomalous dispersion region.

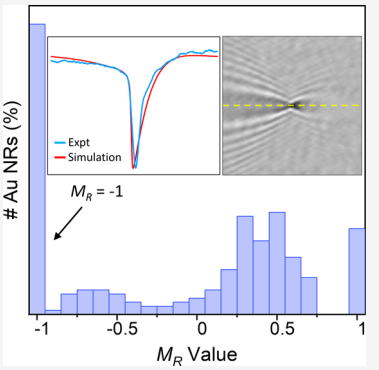

Owing to their unique physical, optical, and chemical properties, plasmonic (e.g., gold and silver) nanorods have attracted significant attention in the areas of biomedical research,[1,2] energy-related science,[3,4] environmental applications,[5,6] etc. For example, gold nanorods (AuNRs) have been utilized in a wide range of applications including biosensing, biomedical imaging, and photothermal therapy.[2,7−9] AuNRs are easily chemically modified via alkanethiol-based attachment chemistries and exhibit both a transverse and a longitudinal localized plasmon resonance that can be used for biosensing or thermal excitation. The longitudinal plasmon resonance extinction (both absorption and scattering) band is very strong and can be tuned from visible to the infrared wavelengths by varying the size and length/width aspect ratio of the nanorod. A thorough understanding of the relationship between the structural and optical properties of AuNRs is essential for a better design of these nanomaterials, and thus it is fundamentally important to develop multiple methods of characterizing single isolated AuNRs without ensemble averaging.

In this paper, we carefully analyze the plasmonic elastic scattering properties of individual AuNRs through the use of single nanoparticle surface plasmon resonance imaging (SPRI) microscopy. SPRI microscopy measurements at 814 nm of single AuNRs in three samples with average longitudinal plasmonic resonance maxima at 670, 816, and 980 nm reveal a variety of diffraction patterns that we can classify with an M_R value based on the intensity and sign of the central peaks in the diffraction image. M_R value histograms for the three samples are quite different, and a unique negative scattering signature is observed from single nanorods when the wavelength of the elastic scattered light is in the anomalous dispersion region, that is, at wavelengths shorter than the peak wavelength of the longitudinal plasmonic resonance maximum.

The transmission electron microscopy (TEM) images and aspect ratio distribution histograms of three different commercially available AuNR samples are shown in Figure 1. TEM data were used to determine that three AuNR samples have average aspect ratios (length in nanometers/width in nanometers = ratio ± standard deviation) of 50.5:19.0 = 2.7 ± 0.5, 44.9:10.7 = 4.2 ± 0.9, and 55.8:9.8 = 5.7 ± 1.2. The UV−visible extinction spectra of the three samples are shown in Figure 2; each spectrum exhibits a strong longitudinal localized plasmonic resonance band with a maximum at 670, 816, and 980 nm, respectively.

The optical absorption and scattering spectra of gold nanorods with different aspect ratios have been calculated previously by Link et al.,[10] Eustis et al.,[11] and other authors.[12,13] The absorption coefficient is calculated using a Gans extension of the Mie scattering theory[14] along with the known complex frequency-dependent dielectric constant of gold, $\epsilon(\omega) = \epsilon'(\omega) + i\epsilon''(\omega)$.[15] For the longitudinal (long axis)

Received: January 25, 2021
Accepted: February 16, 2021

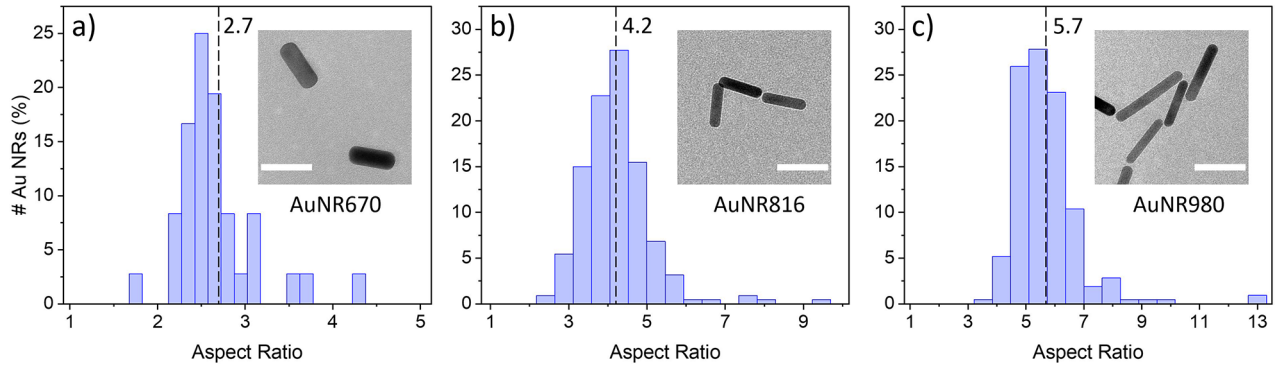

Figure 1. Histograms of aspect ratio distributions of three different AuNR samples (AuNR670, AuNR816, and AuNR980). The dashed lines indicate average aspect ratio values. (insets) The corresponding TEM images of the AuNRs. Scale bars represent 50 nm.

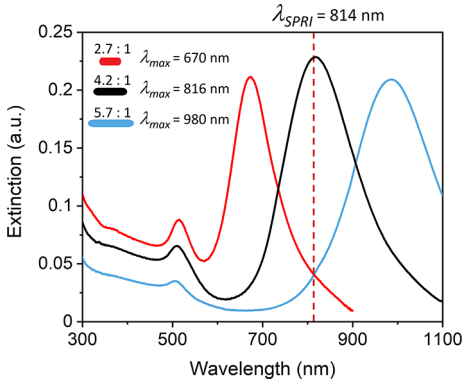

Figure 2. UV−Visible extinction spectra of the three AuNR samples. The average longitudinal plasmonic maxima are located at 670, 816, and 980 nm, respectively. The vertical dashed line at 814 nm indicates the wavelength of the laser used in all of the SPRI microscopy experiments.

resonance of the gold nanorod, the extinction coefficient γ is proportional to

$$\gamma \propto \frac{(\epsilon''/P^2)}{\left[\epsilon' + \frac{1-P}{P}\epsilon_m\right]^2 + \epsilon''^2} \quad (1)$$

and the resonance condition for the extinction coefficient is

$$\epsilon' = \frac{P-1}{P}\epsilon_m \quad (2)$$

where ϵ_m is the dielectric constant of the surrounding medium, and P is a shape factor that depends on the aspect ratio of the nanorod. With this equation, the wavelength of the plasmon resonance maximum was found to vary linearly with the aspect ratio.[10−12] This linear relationship between the average aspect ratios and the wavelength of the longitudinal plasmon resonance maxima is also observed experimentally for the three gold nanorod samples used in this paper.

Additionally, Eustis and El Sayed[11] have shown that the observed longitudinal plasmonic resonance bands for a nanorod sample can be thought of as a set of inhomogeneously broadened bands from individual nanoparticles with different aspect ratios. The single nanoparticle SPRI microscopy measurements described in this paper employed a wavelength λ_{SPRI} of 814 nm. Thus, in the SPRI microscopy measurements: (i) for the 670 nm AuNR sample, most of the nanorods will have a longitudinal surface plasmon resonance maximum at a wavelength above λ_{SPRI}, (ii) for the 980 nm AuNR sample, most of the nanorods will have a resonance maximum at a wavelength below λ_{SPRI}, and (iii) for the 816 nm AuNR sample there will be roughly equal numbers of nanorods with resonance maxima above and below the λ_{SPRI}.

SPRI microscopy has become an extremely useful spectroscopic method for the detection and characterization of the adsorption of single polymeric and metal nanoparticles onto gold thin-film surfaces in real time. As described previously[16] and shown schematically in Figure 3a, SPRI

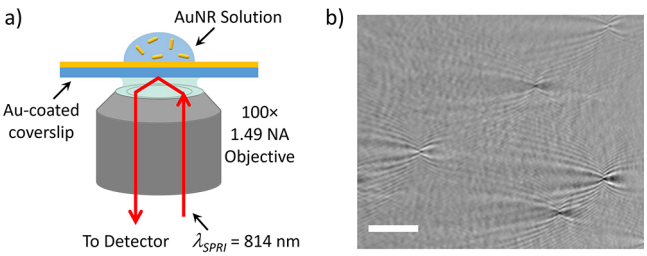

Figure 3. SPRI microscopy measurements of single AuNRs. (a) Schematic diagram of the objective-coupled SPRI microscope. (b) A representative differential SPRI image of 670 nm AuNRs sample. The scale bar represents 10 μm.

differential reflectivity images of gold thin films are captured using a high numerical aperture objective in a total internal reflectance geometry with an off-axis laser source (λ_{SPRI} = 814 nm) set to deliver an incident angle (θ_{in}) that is typically just below the resonant SPR angle (θ_{sp}).[17] The surface plasmon polaritons (SPPs) traveling along the gold surface diffract off of the adsorbed nanoparticles; the diffraction of SPPs into other SPPs traveling in different directions is coupled back out of the prism and combined with the SPR reflected light to create the SPRI diffraction image.[18−21] Single nanoparticle microscopy has been used in a wide variety of applications: the detection of viruses and metallic nanoparticles,[22−25] measurements of the hybridization adsorption of DNA-modified gold nanoparticles (AuNPs),[16] monitoring the uptake of peptides and proteins into porous polymeric nanoparticles,[26,27] detecting quantum tunneling between AuNPs and the gold thin film,[28] the detection of single exosomes and liposomes,[29,30] and the detection of single proteins.[31,32]

SPRI microscopy experiments are used in this paper to monitor the irreversible electrostatic adsorption of AuNRs onto chemically modified gold thin films. As described previously,[16] a series of 200 SPRI differential images were obtained in 10 min (3 s per frame—each differential SPRI

https://dx.doi.org/10.1021/acs.jpclett.1c00268
J. Phys. Chem. Lett. 2021, 12, 2004−2010

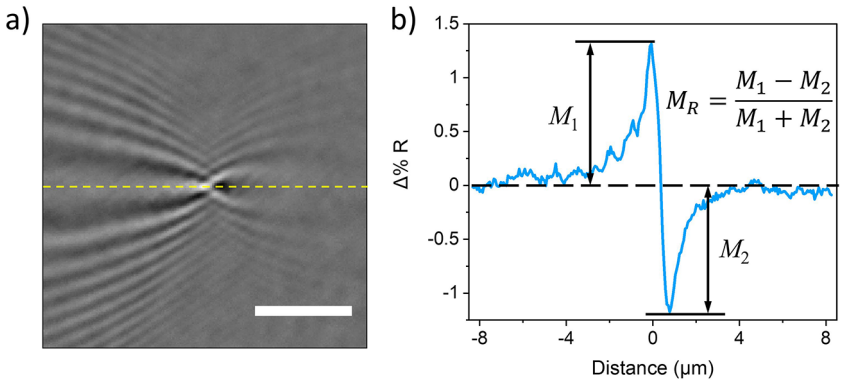

Figure 4. (a) An expanded area view of a AuNR diffraction pattern taken from the 670 nm AuNR sample. The scale bar represents 5 μm. (b) Horizontal intensity profile taken through the center of the diffraction pattern (indicated by the yellow horizontal dashed line) in (a). M_1 and M_2 are the amplitudes of the positive and negative peaks.

images was created by the difference between two sequential SPRI images) as AuNRs were adsorbed from a 10 μL aqueous solution containing either 670, 816, or 980 nm AuNR samples onto a gold thin film. The gold surface was functionalized with an amine-terminated alkanethiol (MUAM) to create a positively charged surface to adsorb the negatively charged AuNRs.[16,30] Each adsorbed AuNR created a diffraction spot that could be counted and quantified. As an example, Figure S1 in the Supporting Information plots the number of adsorbed AuNRs from the 670 nm AuNR sample as a function of time over the course of an SPRI microscopy experiment.

Figure 3b plots a representative three-second AuNR differential SPRI image in which five nanorods from the 670 nm AuNR sample have adsorbed onto the gold surface and created diffraction spots. The direction of plasmon propagation in the SPRI images is from the right to the left. For each nanorod, a large (on the order of tens of microns in length) diffraction pattern with a high-intensity central area and two parabolic patterns extending to both left and right sides with alternating bright and dark tails was observed. However, it is important to note that, in this single image, there are several qualitatively different types of AuNR diffraction patterns. Some have a bright positive spot at the center of the diffraction pattern, some have a dark spot, and some have both. In general, the diffraction pattern and intensity can depend on the shape, size, orientation, and material composition of a nanosized object. The fact that a variety of diffraction patterns can be observed in a single image from different nanorods in the 670 nm AuNR sample is significant and suggests that there is a distribution of AuNRs each with a different characteristic SPRI response.

To further explore the origins of this distributed SPRI response from the AuNRs we must carefully quantitate the types of SPRI diffraction spots observed in each of the SPRI images. Figure 4a is an expanded area view of a AuNR diffraction pattern taken from the 670 nm AuNR sample; Figure 4b is a horizontal line profile taken through the center of the diffraction pattern (the horizontal yellow dashed line shown in Figure 4a). The horizontal cut is 16.6 μm (256 pixels) in length. For this AuNR diffraction spot, the horizontal intensity profile contains both a positive-going peak located at approximately the center of the line and a negative-going peak to the immediate right of the positive peak. The pixel intensities in this paper are reported in units of $\Delta\%R$, which correspond to the percent reflectivity change. We observed that each AuNR diffraction pattern has a unique horizontal intensity profile. In order to quantify the characteristics of the intensity profiles, we introduce a unitless ratio parameter M_R defined as in eq 3:

$$M_R = \frac{M_1 - M_2}{M_1 + M_2} \tag{3}$$

where M_1 and M_2 are the amplitudes of the positive and negative peaks as described in Figure 4b. A positive M_R value indicates that the magnitude of the positive-going peak is greater than that of the negative-going peak and vice versa. The M_R value has a total range of $\{1$ to $-1\}$: $M_R = 1$ when there is only a positive peak ($M_2 = 0$), to $M_R = -1$ when there is only a negative peak present ($M_1 = 0$).

Histograms showing the distribution of M_R values observed for diffraction patterns from each of the three AuNR samples were calculated; Figure 5 shows the M_R value histogram for the 670 nm AuNR samples. As seen in Figure 5, 30% of all observed diffraction spots were classified as $M_R = -1$ for the 670 nm AuNR sample. The first inset in Figure 5 shows the average horizontal profile for the $M_R = -1$ diffraction spots: a single negative peak at the M_2 position in horizontal intensity

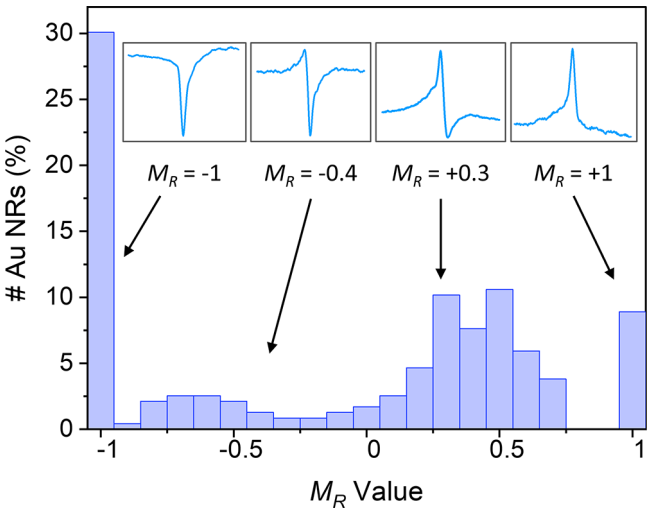

Figure 5. M_R value distribution histogram obtained from the SPRI diffraction patterns of 670 nm AuNRs. A total number of 236 AuNRs were analyzed. (insets) The average horizontal profiles for diffraction spots with various M_R values.

https://dx.doi.org/10.1021/acs.jpclett.1c00268
J. Phys. Chem. Lett. 2021, 12, 2004−2010

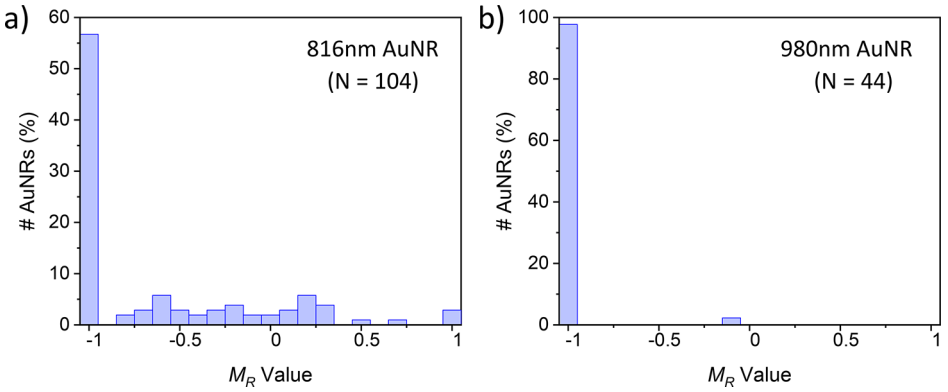

Figure 6. M_R value distribution histograms obtained from the SPRI diffraction patterns from (a) the 816 nm AuNR sample and (b) the 980 nm AuNR sample. *N* is the total number of AuNRs analyzed for each sample.

profile. The other insets in the figure show some of the other types of horizontal profiles obtained for diffraction patterns with $M_R = -0.4$, 0.3, and 1. Approximately 50% of the diffraction spots had an $M_R > 0$, with a median value of $M_R = 0.5$. Only ~10% had an $M_R = 1$ value.

Figure 6 shows the M_R value histograms for the 816 and 980 nm AuNR samples, and Table 1 tabulates the M_R values taken from the histograms for the three AuNR samples. For the 816 nm AuNR sample, 57% of the diffraction spots have an M_R value of −1; for the 980 nm AuNR sample, 98% of the diffraction spots have an M_R value of −1.

Table 1. M_R Value Distribution for the 670, 816, and 980 nm AuNR Samples

M_R value	670 nm AuNR	816 nm AuNR	980 nm AuNR
−1	30%	57%	98%
$0 \geq M_R > -1$	16%	26%	2%
$1 > M_R > 0$	45%	14%	0%
+1	9%	3%	0%

The large diversity of M_R ratios observed from the AuNR samples differs from that seen in SPRI microscopy experiments from other nanoparticles. For polymer (e.g., polystyrene, latex) nanoparticles, only $M_R = 1$ values have been observed,[20,30] whereas for AuNPs a biphasic behavior with $M_R = +0.2$ has been observed.[33] (Please see Figure S2 in the Supporting Information for an example).

Only the AuNRs exhibit this unique $M_R = -1$ behavior with a single negative peak at the M_2 location. However, it is important to note that slightly different types of negative point diffraction patterns have been observed previously in SPRI microscopy experiments. For example, negative point diffraction patterns have been observed from gas-containing nanoparticles due to a decrease in the local refractive index created by the replacement of aqueous solution.[30] Negative point diffraction patterns have also been observed when a particle desorbs from a surface after adsorption. In both of these cases, the negative peak occurs at the M_1 location. Moreover, for adsorption−desorption pairs, there is always a positive peak diffraction pattern due to the adsorption of the nanoparticle that appears prior to the negative diffraction peak.

A very important observation about the $M_R = -1$ diffraction peaks comes to light when comparing the three AuNR samples. The percentage of $M_R = -1$ values follows the trend: 30%:57%:98% for 670 nm/816 nm/980 nm AuNR samples (Table 1). This trend is in agreement with the earlier discussion on the correlation of the number of nanorods in a AuNR sample with the position of the plasmon resonance band wavelength maximum relative to the laser wavelength used in the SPRI microscopy experiments. For example, the 814 nm wavelength of the laser used in the SPRI microscopy experiments is almost exactly equal to the maximum of the plasmonic resonance band at 816 nm observed in Figure 2; for this case, 57% of the AuNRs have a diffraction pattern with an M_R value of −1. The plasmon band at 816 nm is due to a strong resonant increase in the imaginary part of the complex dielectric constant of the sample; as shown using Kramers−Kronig relations,[34] concomitant with this increase there is a differential change in the real part of the complex dielectric constant, where it decreases at photon energies above (and thus at wavelengths shorter than) the resonance band. This wavelength region is called the anomalous dispersion region due to the well-known decrease in the refractive index (which is the square root of the dielectric constant) at these wavelengths.[35] This suggests that the negative diffraction spots are due to AuNRs with plasmonic resonances that place the 814 nm in the anomalous dispersion region. For the 980 nm AuNR sample, the 814 nm laser wavelength is significantly above the average plasmonic resonance extinction maximum, and thus virtually all (98%) of the M_R values for the 980 nm AuNR sample are equal to −1. In contrast, the reverse is observed for the 670 nm AuNR sample, where only 30% of the M_R values are equal to −1, since the average plasmonic resonance extinction maximum wavelength is shorter than the 814 nm laser wavelength.

To fit the biphasic gold nanorod diffraction data in our SPRI microscopy measurements, we use an extension of the plasmonic scattering model proposed by Yu *et al.*[19,20] In this model, the differential SPRI image $I_d(x,y)$ is created from the interference of the partially reflected field and scattered plasmonic field in the direction of reflection

$$I_d(x, y) = |E_r + E_{sc}|^2 - |E_r|^2 \quad (4)$$

where E_r is the reflected wave obtained from the incident wave E_{in} at the angle θ_{in}, and E_{sc} is the light that is scattered off the nanorod into the surface plasmon channel and then coupled back out through the gold thin film and prism at the SPR resonance angle θ_{sp}. The magnitude and phase of E_r is related to E_{in} via the complex Fresnel coefficient r_p from a three-phase (BK7/gold thin film/water) Fresnel reflectance calculation

https://dx.doi.org/10.1021/acs.jpclett.1c00268
J. Phys. Chem. Lett. 2021, 12, 2004−2010

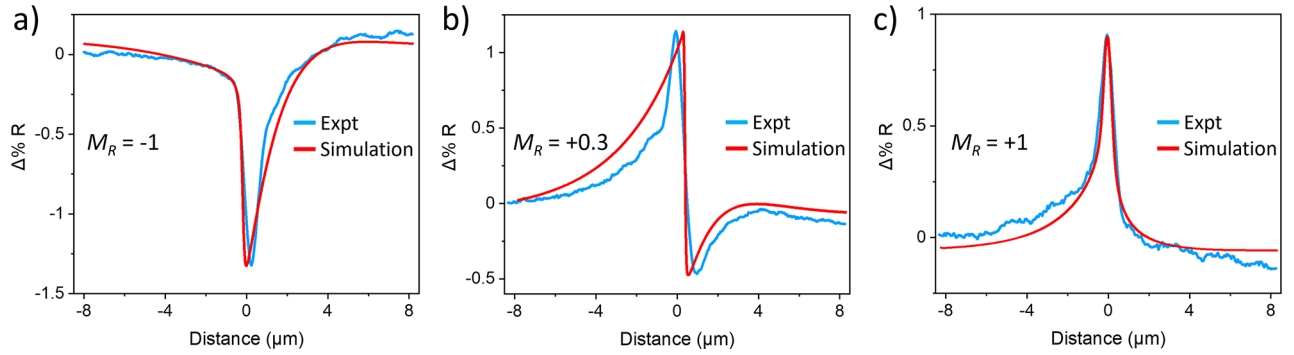

Figure 7. Theoretical fits of AuNR diffraction images. Three representative horizontal center line plots are simulated (red lines) and compared with experimental data (blue lines) from 670 nm AuNRs. M_R values are (a) −1, (b) +0.3, and (c) +1. A variety of M_R values from −1 to 1 is observed for AuNRs, depending on the relative position of the resonance band of a specific AuNR as compared to the laser wavelength used in the SPRI microscopy experiments (814 nm).

$$E_r = r_p E_{in}\, e^{+ik_{in}x} \quad k_{in} = k_1 \sin\theta_{in} \tag{5}$$

where k_1 is the wavevector of the 814 nm light in the prism.

The scattered light E_{sc} has been previously modeled as a convolution of a two-dimensional Gaussian point spread function (O) with an isotropic point scattering function (h) that includes a complex scattering coefficient (α). To fit the biphasic gold nanorod data, we expand this definition to include an anisotropic point scattering function that is different in the forward ($x < 0$) and reverse ($x > 0$) scattering directions.

$$E_{sc} = O^{*}h \tag{6}$$

$$h = E^0\alpha_1\, e^{-k_{d1}r}\, e^{-ik_{sp1}r} \quad x < 0 \tag{7}$$

$$h = E^0\alpha_2\, e^{-k_{d2}r}\, e^{+ik_{sp2}r} \quad x \geq 0 \tag{8}$$

where E^0 is the driving surface plasmon field created by the incident wave at the location of the nanorod, $k_{d1}$and k_{d2} are decay constants of surface plasmons, $k_{sp1}$and k_{sp2} are wavevectors of surface plasmons, and r is the distance to the scatterer. The anisotropic scattering function h now includes different complex scattering coefficients α_1 and α_2, in the forward and reverse directions, respectively. We define α_1 and α_2 as

$$\alpha_1 = \alpha'_1 + i\alpha''_1 = |\alpha_1|(\cos\phi_1 + i\sin\phi_1) \tag{9}$$

$$\alpha_2 = \alpha'_2 + i\alpha''_2 = |\alpha_2|(\cos\phi_2 + i\sin\phi_2) \tag{10}$$

where ϕ_1 and ϕ_2 are the phases of α_1 and α_2 in polar coordinates. Using this model, we can calculate the diffraction images and the center line plots used to determine the M_R value for a diffraction spot. Figure 7 shows theoretical calculations (red lines) of the center line intensity plots along with the experimental data for diffraction spots with three typical M_R values of −1, +0.3, and +1. The positive, biphasic, and negative central diffraction peaks can be successfully simulated, and the excellent agreement between the theoretical fits and the experimental results validates our model employing anisotropic scattering coefficients. Table 2 lists the ϕ_1 and ϕ_2 values used in our calculations and the signs of the real and imaginary parts of α_1 and α_2. A complete list of the actual parameter values used in the theoretical fits is given in Table S1 in the Supporting Information. From Table 2 it is clear that the signs of the scattering coefficients α_1 and α_2 are uniquely negative for the case of $M_R = -1$.

Table 2. Parameters Used in Theoretical Fittings of AuNR Diffraction Images with Different M_R Values

M_R value	ϕ_1	ϕ_2	α_1'	α_1''	α_2'	α_2''
−1	~3π/2	~π	0	−	−	0
+0.3	0	4π/3	+	0	−	−
+1	π/3	5π/3	+	+	+	−

In summary, we have observed a complex resonant scattering behavior in the SPRI microscopy measurements of single AuNRs at wavelengths near the longitudinal plasmonic resonance band maximum. The parameter M_R is introduced to quantify the characteristics of the intensity profiles of central peaks in the diffraction images. For AuNRs, a variety of M_R values ranging from −1 to +1 were observed. This range of M_R values is attributed to the fact that (i) the scattering coefficient for a AuNR is both complex and anisotropic and (ii) the values of the AuNR scattering coefficient is sensitive to the position of the AuNR plasmonic resonance extinction maxima relative to the SPRI laser wavelength. For polymeric nanoparticles, only $M_R = 1$ values are observed. In contrast, the AuNRs exhibit a unique $M_R = -1$ scattering signature when the wavelength of the SPRI microscopy experiment λ_{SPRI} is in the anomalous dispersion region of the resonance of that specific AuNR. For the diffraction patterns of AuNRs with an M_R value of −1 the center line plots of the diffraction images can be fit with an anisotropic complex scattering coefficient that is uniquely negative. We anticipate that the unique scattering properties of AuNRs can be useful for identifying specific nanorods in biosensing and high-throughput screening systems.

Finally, it must be noted that the SPRI microscopy scattering from these plasmonic nanorods is undoubtedly influenced by the coupling between the localized SPR resonance of the AuNR and the planar traveling surface plasmon polaritons at 814 nm. A recent paper in 2020 by Tao et al.[26] showed that, for AuNPs, the diffraction pattern could vary quickly on the tens of milliseconds time scale approximately between M_R values of +0.2 and −0.2 due to changes in the nature of this coupling based on the distance from the gold surface. These distance effects are certainly present in the AuNRs, but the time scale (3 s per image) of our experiments perhaps prevents us from seeing them. Also, the SPRI microscopy scattering from AuNPs can be described with an average M_R of 0.2 (see Figure S2); however, an $M_R = -1$ for AuNPs is never observed. Thus, we conclude that an M_R value of −1 is a unique behavior of the resonant SPRI microscopy scattering response. Future

https://dx.doi.org/10.1021/acs.jpclett.1c00268
J. Phys. Chem. Lett. 2021, 12, 2004−2010

experiments of the SPRI scattering of AuNRs from gold surfaces with precise polyelectrolyte layer-by-layer (LbL) multilayer coatings that can control the distance between the electrostatically adsorbed AuNRs and the gold surface will be used to further explore localized SPR-planar SPR coupling effects.

■ ASSOCIATED CONTENT

Supporting Information

The Supporting Information is available free of charge at https://pubs.acs.org/doi/10.1021/acs.jpclett.1c00268.

Experimental methods, AuNR adsorption curve as a function of time, diffraction pattern of a spherical AuNP, and list of parameters used for theoretical calculations (PDF)

■ AUTHOR INFORMATION

Corresponding Author

Robert M. Corn − *Department of Chemistry, University of California-Irvine, Irvine, California 92697, United States;* orcid.org/0000-0002-4756-2161; Email: rcorn@uci.edu

Authors

Yunshan Fan − *Department of Chemistry, University of California-Irvine, Irvine, California 92697, United States*

Yara Aceta − *Department of Chemistry, University of California-Irvine, Irvine, California 92697, United States*

Esther Hessong − *Department of Chemistry, University of California-Irvine, Irvine, California 92697, United States*

Athena Bengston − *Department of Chemistry, University of California-Irvine, Irvine, California 92697, United States*

Laris A. Biageyian − *Department of Chemistry, University of California-Irvine, Irvine, California 92697, United States*

Quan P. Huynh − *Department of Chemistry, University of California-Irvine, Irvine, California 92697, United States*

Complete contact information is available at: https://pubs.acs.org/10.1021/acs.jpclett.1c00268

Notes

The authors declare no competing financial interest.

■ ACKNOWLEDGMENTS

This work was supported by the Chemistry Division of the National Science Foundation, Grant No. CHE-1807317. We thank C. Qian and Prof. M. Law at UCI for their UV−vis spectrometer and Prof. H. Yu at Shanghai Jiao Tong University for helpful discussions and reprints.

■ REFERENCES

(1) Salem, A. K.; Searson, P. C.; Leong, K. W. Multifunctional nanorods for gene delivery. *Nat. Mater.* **2003**, *2*, 668−671.

(2) Cao, J.; Sun, T.; Grattan, K. T. V. Gold nanorod-based localized surface plasmon resonance biosensors: A review. *Sens. Actuators, B* **2014**, *195*, 332−351.

(3) Manthiram, A.; Vadivel Murugan, A.; Sarkar, A.; Muraliganth, T. Nanostructured electrode materials for electrochemical energy storage and conversion. *Energy Environ. Sci.* **2008**, *1*, 621−638.

(4) Huynh, W. U.; Dittmer, J. J.; Alivisatos, A. P. Hybrid nanorod-polymer solar cells. *Science* **2002**, *295*, 2425−2427.

(5) Noh, J. S.; Lee, J. M.; Lee, W. Low-Dimensional Palladium Nanostructures for Fast and Reliable Hydrogen Gas Detection. *Sensors* **2011**, *11*, 825−851.

(6) Li, Y. F.; Cui, F.; Ross, M. B.; Kim, D.; Sun, Y.; Yang, P. D. Structure-Sensitive CO_2 Electroreduction to Hydrocarbons on Ultrathin 5-fold Twinned Copper Nanowires. *Nano Lett.* **2017**, *17*, 1312−1317.

(7) Huang, X.; Neretina, S.; El-Sayed, M. A. Gold nanorods: from synthesis and properties to biological and biomedical applications. *Adv. Mater.* **2009**, *21*, 4880−4910.

(8) Huang, X. H.; El-Sayed, I. H.; Qian, W.; El-Sayed, M. A. Cancer cell imaging and photothermal therapy in the near-infrared region by using gold nanorods. *J. Am. Chem. Soc.* **2006**, *128*, 2115−2120.

(9) Zhang, Z. J.; Wang, L. M.; Wang, J.; Jiang, X. M.; Li, X. H.; Hu, Z. J.; Ji, Y. H.; Wu, X. C.; Chen, C. Y. Mesoporous Silica-Coated Gold Nanorods as a Light-Mediated Multifunctional Theranostic Platform for Cancer Treatment. *Adv. Mater.* **2012**, *24*, 1418−1423.

(10) Link, S.; Mohamed, M. B.; El-Sayed, M. A. Simulation of the optical absorption spectra of gold nanorods as a function of their aspect ratio and the effect of the medium dielectric constant. *J. Phys. Chem. B* **1999**, *103*, 3073−3077.

(11) Eustis, S.; El-Sayed, M. A. Determination of the aspect ratio statistical distribution of gold nanorods in solution from a theoretical fit of the observed inhomogeneously broadened longitudinal plasmon resonance absorption spectrum. *J. Appl. Phys.* **2006**, *100*, 044324.

(12) Jain, P. K.; Lee, K. S.; El-Sayed, I. H.; El-Sayed, M. A. Calculated absorption and scattering properties of gold nanoparticles of different size, shape, and composition: Applications in biological imaging and biomedicine. *J. Phys. Chem. B* **2006**, *110*, 7238−7248.

(13) Lee, K. S.; El-Sayed, M. A. Dependence of the enhanced optical scattering efficiency relative to that of absorption for gold metal nanorods on aspect ratio, size, end-cap shape, and medium refractive index. *J. Phys. Chem. B* **2005**, *109*, 20331−20338.

(14) Papavassiliou, G. C. Optical-Properties of Small Inorganic and Organic Metal Particles. *Prog. Solid State Chem.* **1979**, *12*, 185−271.

(15) Johnson, P. B.; Christy, R. W. Optical Constants of Noble Metals. *Phys. Rev. B* **1972**, *6*, 4370−4379.

(16) Halpern, A. R.; Wood, J. B.; Wang, Y.; Corn, R. M. Single-Nanoparticle Near-Infrared Surface Plasmon Resonance Microscopy for Real-Time Measurements of DNA Hybridization Adsorption. *ACS Nano* **2014**, *8*, 1022−1030.

(17) Huang, B.; Yu, F.; Zare, R. N. Surface plasmon resonance imaging using a high numerical aperture microscope objective. *Anal. Chem.* **2007**, *79*, 2979−2983.

(18) Demetriadou, A.; Kornyshev, A. A. Principles of nanoparticle imaging using surface plasmons. *New J. Phys.* **2015**, *17*, 013041.

(19) Yu, H.; Shan, X. N.; Wang, S. P.; Chen, H. Y.; Tao, N. J. Molecular Scale Origin of Surface Plasmon Resonance Biosensors. *Anal. Chem.* **2014**, *86*, 8992−8997.

(20) Yu, H.; Shan, X. N.; Wang, S. P.; Tao, N. J. Achieving High Spatial Resolution Surface Plasmon Resonance Microscopy with Image Reconstruction. *Anal. Chem.* **2017**, *89*, 2704−2707.

(21) Yang, Y. T.; Zhai, C. H.; Zeng, Q.; Khan, A.; Yu, H. Quantitative Amplitude and Phase Imaging with Interferometric Plasmonic Microscopy. *ACS Nano* **2019**, *13*, 13595−13601.

(22) Wang, S. P.; Shan, X. N.; Patel, U.; Huang, X. P.; Lu, J.; Li, J. H.; Tao, N. J. Label-free imaging, detection, and mass measurement of single viruses by surface plasmon resonance. *Proc. Natl. Acad. Sci. U. S. A.* **2010**, *107*, 16028−16032.

(23) Wang, W.; Tao, N. J. Detection, Counting, and Imaging of Single Nanoparticles. *Anal. Chem.* **2014**, *86*, 2−14.

(24) Weichert, F.; Gaspar, M.; Timm, C.; Zybin, A.; Gurevich, E.; Engel, M.; Muller, H.; Marwedel, P. Signal Analysis and Classification for Surface Plasmon Assisted Microscopy of Nanoobjects. *Sens. Actuators, B* **2010**, *151*, 281−290.

(25) Zybin, A.; Kuritsyn, Y. A.; Gurevich, E. L.; Temchura, V. V.; Uberla, K.; Niemax, K. Real-time Detection of Single Immobilized Nanoparticles by Surface Plasmon Resonance Imaging. *Plasmonics* **2010**, *5*, 31−35.

(26) Cho, K.; Fasoli, J. B.; Yoshimatsu, K.; Shea, K. J.; Corn, R. M. Measuring Melittin Uptake into Hydrogel Nanoparticles with Near-

Infrared Single Nanoparticle Surface Plasmon Resonance Microscopy. *Anal. Chem.* **2015**, *87*, 4973−4979.
(27) Maley, A. M.; Terada, Y.; Onogi, S.; Shea, K. J.; Miura, Y.; Corn, R. M. Measuring Protein Binding to Individual Hydrogel Nanoparticles with Single-Nanoparticle Surface Plasmon Resonance Imaging Microscopy. *J. Phys. Chem. C* **2016**, *120*, 16843−16849.
(28) Wang, H.; Yu, H.; Wang, Y.; Shan, X. N.; Chen, H. Y.; Tao, N. J. Phase imaging of transition from classical to quantum plasmonic couplings between a metal nanoparticle and a metal surface. *Proc. Natl. Acad. Sci. U. S. A.* **2020**, *117*, 17564−17570.
(29) Yang, Y. T.; Shen, G. X.; Wang, H.; Li, H. X.; Zhang, T.; Tao, N. J.; Ding, X. T.; Yu, H. Interferometric plasmonic imaging and detection of single exosomes. *Proc. Natl. Acad. Sci. U. S. A.* **2018**, *115*, 10275−10280.
(30) Viitala, L.; Maley, A. M.; Fung, H. W. M.; Corn, R. M.; Viitala, T.; Murtomaki, L. Surface Plasmon Resonance Imaging Microscopy of Liposomes and Liposome-Encapsulated Gold Nanoparticles. *J. Phys. Chem. C* **2016**, *120*, 25958−25966.
(31) Zhang, P. F.; Ma, G. Z.; Dong, W.; Wan, Z. J.; Wang, S. P.; Tao, N. J. Plasmonic scattering imaging of single proteins and binding kinetics. *Nat. Methods* **2020**, *17*, 1010−1017.
(32) Maley, A. M.; Lu, G. J.; Shapiro, M. G.; Corn, R. M. Characterizing Single Polymeric and Protein Nanoparticles with Surface Plasmon Resonance Imaging Measurements. *ACS Nano* **2017**, *11*, 7447−7456.
(33) Qian, C.; Wu, G.; Jiang, D.; Zhao, X. N.; Chen, H. B.; Yang, Y. Z.; Liu, X. W. Identification of Nanoparticles via Plasmonic Scattering Interferometry. *Angew. Chem., Int. Ed.* **2019**, *58*, 4217−4220.
(34) Lucarini, V.; Saarinen, J. J.; Peiponen, K.-E.; Vartiainen, E. M. *Kramers-Kronig Relations in Optical Materials Research;* Springer: Germany, 2005.
(35) Sommerfeld, A. *Optics;* Academic Press, 1964.

https://dx.doi.org/10.1021/acs.jpclett.1c00268
J. Phys. Chem. Lett. 2021, 12, 2004−2010